

Abstract

Theoretical condensed matter research is plagued by a fundamental issue of complexity. The sheer amount of degrees of freedom in a material on any technologically relevant scale is overwhelming (e.g. $\sim 10^{23}$ electrons per cm^3), and makes it impossible to describe the quantum mechanical wavefunction exactly.

The Hamiltonian plays a central role in the description of crystals, the subject of this thesis. It can be decomposed into various parts, and their interactions. Depending on the physics under scrutiny it then often suffices to solve only one of those parts. This can be either because the energy scales and associated timescales that govern the constituents are very different, or because the interactions between them are small. One example, often put into practice, is the separation of electronic and phononic (lattice) degrees of freedom, leading to the well-known Born-Oppenheimer approximation, decoupling their respective motion. Another is the often neglected spin-orbit coupling, due to the tiny prefactor associated with its relativistic origin.

Solving these subproblems then allows for progress to be made in understanding the physics that govern them. However, there will inevitably be systems for which this interaction is not small and leads to fascinating new physics that manifestly depends on both subsystems combined. In this thesis we focus on these cases and how they arise in functional materials, with the occasional eye towards applications in technology.

The reason why these cross-order couplings can be interesting for technological applications, is that often one of the orders is more robust with respect to perturbations, and therefore more long-lived, but also harder to control efficiently. By exploiting the cross-order coupling in certain materials, one could potentially control the long lived order by applying perturbations to the more easily controllable order.

In giant Rashba effect systems, the coupling between spin and ferroelectric order leads to a linear spin-splitting of the band structure, whose sign depends on the orientation of the ferroelectric polarization. We show that, rather than the relativistic Rashba effect, a combination of electrostatics and atomic spin-orbit coupling lies at the origin of the large splitting.

The coupling between magnetism and ferroelectricity in multiferroic GdMn_2O_5 leads to a never before observed four-state hysteresis loop for the ferroelectric polarization, which depends on the magnitude, angle and history of the applied magnetic field. As we will show, this four-state hysteresis loop is accompanied by a full 360° rotation of spins in the material, which resembles the crankshaft of a car, converting the linear back-and-forth motion of the magnetic field into a rotational motion of the spins.

In a thin film of elemental Chromium, the ultrafast dynamics of a spin

density wave, coupled to a slower varying charge density wave, allows for a high degree of control of the latter through excitations of the former. This allows us to predict the sequence of optical pulses to be applied to the material in order to follow closely an enveloping signal function.

And finally, the coupling between ferroelectricity and strain in BaTiO₃ leads to a softening at purely ferroelectric domain walls, allowing for some mechanical control of the position of this wall.

We utilize both theoretical and computational tools to understand the nature of these interactions, how they lead to cross-order coupling in these materials, and how this then translates into the experimentally observed behavior.

Chapter 1

Spin-momentum locking in high spin-orbit coupled ferroelectrics

1.1 Introduction

The research field of spintronics aims to understand the behavior of spins inside materials, and translate this understanding into active control of these degrees of freedom for possible technological applications. Many possible devices have been theorized for example are spin field-effect transistors (spin-FET)[**Datta1990**] and storage devices which utilize spin-current and associated spin-transfer torque to efficiently manipulate magnetic domains [**Kent2015**, **Jungwirth2016**]. In spite of fundamental interest and potential for applications, the actual realization of these devices has been rather elusive. One of the main culprits for the limited success to date is that the devices require very granular, ideally electric, control of the spin, which is impeded by widely separated energy scales and weak coupling between magnetic and charge degrees of freedom. One class of materials that allows for such electric control of spin-polarized states are the ferroelectric semiconductors with large atomic spin-orbit coupling (SOC) [**DiSante2013**, **Ishizaka2011**, **Kim2014**]. Inversion symmetry breaking together with SOC results in a linear splitting of spin-polarized bands, seen in the band structure as a conical intersection surrounding a high-symmetry point of the Brillouin Zone (see Fig. ??). Thus, current carriers (holes in the case of Fig. ??) travelling through the material will tend to align their spins to these spin-polarized bands. As we discuss in more detail in the following, the direction of the spin polarization depends on the orientation and strength of the electric field \mathbf{E} . In ferroelectrics, an internal field results from the polarization P , allowing it to be tuned and switched by an external applied electric field. These spin-polarized states have been observed both experimentally [**Ishizaka2011**, **Liebmann2016**, **Krempasky2015SurfaceSemiconductor**], and from *ab initio* density functional theory (DFT) simulations [**DiSante2013**]. It is, however, often not well understood and often misattributed what the underlying microscopic mechanisms are that lead to the observed splitting. [explicit men-

tions? Maybe too aggressive]

We investigate multiple different origins of this k and E dependent spin-splitting. The discussed contributions arise due to the Hamiltonian of form

$$H_R(\mathbf{k}) = \alpha_R \frac{\mathbf{E}}{|\mathbf{E}|} \cdot (\mathbf{k} \times \hat{\sigma}), \quad (1.1)$$

where $\hat{\sigma}$ is the electron spin operator, and \mathbf{E} the electric field. It will turn out that multiple microscopic effects can lead to contributions of this form, some of these are well known, others are more obscure. The magnitude of the contribution depends on the microscopic origin, namely whether the effect is purely relativistic or rather a combination of relativistic and electrostatic. Certain materials showcase an exceedingly big splitting, for example in GeTe as can be seen in Fig. ??, and will be used as the main example throughout this chapter.

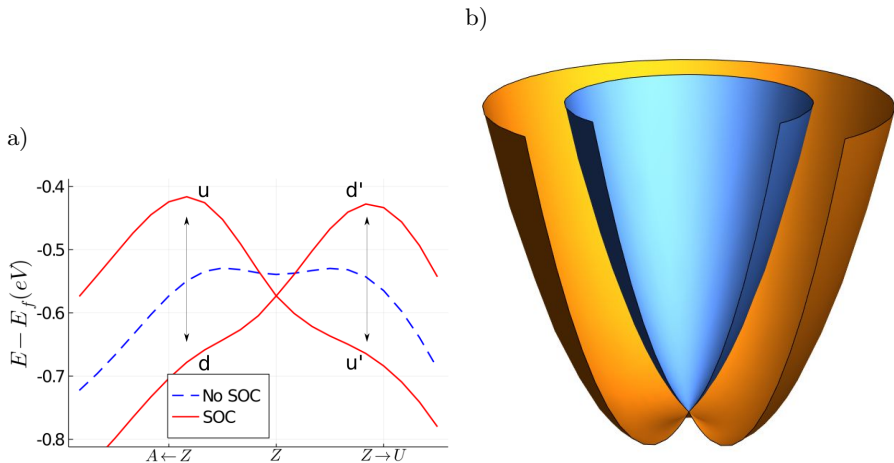


Figure 1.1: **Large Rashba splitting** (a) The band dispersion of the first valence band in GeTe, around the Z -point of the Brillouin zone (see Fig. ?? for details). Two graphs show both non spin-orbit coupled (NSOC, blue), and spin-orbit coupled (SOC, red) case. The $u-d$ and $u'-d'$ labels designate the up and down spin-polarized bands, where the prime signifies that the orientation of the spin axis depends on specific path followed in k -space. b) Shifted parabolic energy levels due to Rashba splitting, and associated spin texture.

We hope that this will shed light on where these contributions come from and how they compare with each other and how they ultimately lead to the observed spin-splitting.

1.2 Rashba-Bychkov Effect

The first discovered and most well known effect bearing the form of Eq. ?? is the Rashba-Bychkov effect, first derived in their seminal 1959 paper [**Rashba1959SymmetryAr**]. It is a relativistic effect that is derived from an expansion to second order in $1/c$, c denoting the speed of light, of the electronic Dirac equation (where the Fouldy-Wouthuysen transformation was applied):

$$\mathcal{H}\psi = \left[\frac{\mathbf{p}^2}{2m} - eV - \frac{e\hbar}{4m^2c^2}(\boldsymbol{\sigma} \cdot [\nabla V \times \mathbf{p}]) - \frac{\hbar^2}{8m^2c^2}\Delta V - \frac{\mathbf{p}^4}{8m^3c^2} \right] \psi = E\psi \quad (1.2)$$

where ψ is a two component spinor, V denotes the electric potential, $\boldsymbol{\sigma}$ a vector of Pauli-matrices ($\sigma_x, \sigma_y, \sigma_z$), m and e the electron mass and charge respectively, and \mathbf{p} the canonical momentum. The first two terms are the nonrelativistic part of the Hamiltonian, the third represents the SOC, the fourth is known as the Darwin effect and the fifth is the relativistic correction to the effective electron mass. As is common in literature, we introduce the spin-orbit coupling constant $\lambda = \frac{e\hbar}{4m^2c^2}$. In a crystal with a periodic potential $V(\mathbf{r})$, electronic wavefunctions are Bloch wavefunctions $\psi_n(\mathbf{k}, \mathbf{r}) = u_n(\mathbf{k}, \mathbf{r})e^{i\mathbf{k}\cdot\mathbf{r}}$, where u_n denotes the cell-periodic part, and n is the band index. To obtain the eigenvalue equation for $u_n(\mathbf{k}, \mathbf{r})$, we insert ψ_n in Eq. ??, and carry out the differentiation $\mathbf{p}e^{i\mathbf{k}\cdot\mathbf{r}}u_n(\mathbf{k}, \mathbf{r}) = e^{i\mathbf{k}\cdot\mathbf{r}}(\mathbf{p} + \mathbf{k})u_n(\mathbf{k}, \mathbf{r})$, and similarly $\mathbf{p}^2 \rightarrow (\mathbf{p} + \mathbf{k})^2$. This leads to the following equation for $u_n(\mathbf{k}, \mathbf{r})$:

$$E_n u_n(\mathbf{k}, \mathbf{r}) = (V_0 + V_1 + V_2 + V_3) u_n(\mathbf{k}, \mathbf{r}) \quad (1.3)$$

$$V_0(\mathbf{k}) = \frac{\mathbf{p}^2}{2m} - eV + \frac{\hbar^2 k^2}{2m} \quad (1.4)$$

$$V_1(\mathbf{k}) = \hbar \frac{\mathbf{k} \cdot \mathbf{p}}{m} \quad (1.5)$$

$$V_2(\mathbf{k}) = -\lambda \boldsymbol{\sigma} \cdot (\nabla V \times \mathbf{k}) \quad (1.6)$$

$$V_3(\mathbf{k}) = -\lambda \boldsymbol{\sigma} \cdot (\nabla V \times \mathbf{p}). \quad (1.7)$$

We neglected the last two terms of Eq. ?? since they are exceedingly small and don't contribute to the linear form of Eq. ???. It is important to understand how the electric fields inside the crystal contribute to V_2 and V_3 , where both terms originate from the application of \mathbf{p} to either $u_n(\mathbf{k}, \mathbf{r})$ or $e^{i\mathbf{k}\cdot\mathbf{r}}$, respectively. We first separate ∇V in two contributions, one coming from the potential wells created by the atoms, and another originating from the ferroelectric polarization (it is assumed that no external fields are applied):

$$\nabla V = \mathbf{E} = \mathbf{E}_{at} + \mathbf{E}_P \quad (1.8)$$

These contributions, together with the two parts of the Bloch functions (i.e. the cell periodic $u_n(\mathbf{k}, \mathbf{r})$, and envelope function $e^{i\mathbf{k}\cdot\mathbf{r}}$) are pictorially shown in Fig. ??.

Looking at the picture, it becomes clear that the contribution of the atomic potential applied to the envelope function is zero because while k is a constant, E_{at} is odd throughout the unit cell, leading to the contributions on either side of the potential well to cancel out. Thus the only contribution to the first term in Eq. ?? comes from the uniform (even) E_P , which in general is very small compared to the atomic one. A similar argument can be applied to the contribution to V_3 . Due to the shape of the periodic part of the wavefunction, only the contribution coming from E_{at} will be nonzero, this is essentially the well-known atomic spin-orbit coupling and can be rather large.

In the following it is assumed that Eq. ?? can be solved for a time reversal (TR) invariant point \mathbf{k}_0 in the first BZ, where the two spin states are necessarily

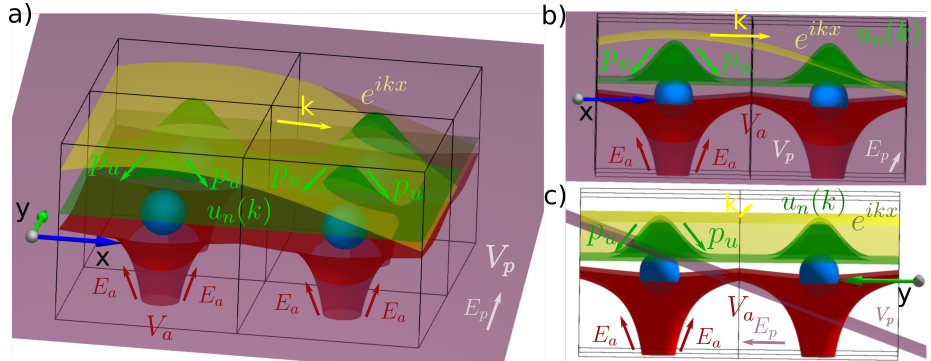


Figure 1.2: Pictorial representation of the different electric potentials (V) and fields (E) in a 2D square lattice. The blue spheres show the atoms, which produce the spherically symmetric red potential V_a and field E_a . The purple slab denotes a uniform ferroelectric polarization potential V_p which in this case is directed along the crystalline y -direction, creating field E_p . The green and yellow surfaces denote two components of the Bloch function: $u_n(k)e^{ikx}$, where the yellow is the envelope plane wave part and the green the cell periodic part. k and p_u denote the two components to the momentum of the bloch function, the former from the envelope function, and the latter the contribution from the periodic part.

degenerate. Due to the broken inversion symmetry and inclusion of the SOC terms (V_2, V_3), this degeneracy will be broken for k points away from the TR invariant point. We denote the two degenerate states at \mathbf{k}_0 by $|u_n^\downarrow\rangle$ and $|u_n^\uparrow\rangle$. It is important to realize that the orientation of spin axis of the eigenstates of Eq. ?? depends on the direction of both \mathbf{k} and \mathbf{P} , as will become clear later. Without loss of generality we take $\mathbf{k}_0 = \mathbf{0}$ and $E_n^{\uparrow\downarrow}(\mathbf{0}) = 0$. Expanding in the deviation away from the high-symmetry point, in the usual $\mathbf{k} \cdot \mathbf{p}$ sense, and keeping only linear \mathbf{k} terms and terms up to second order in $1/c$, we get

$$E_n^{\sigma_1}(\mathbf{k}) = -V_2^{\sigma_1}(\mathbf{k}) + \quad (1.9)$$

$$\sum_{m,\sigma_2=\uparrow,\downarrow} \frac{\langle u_n^{\sigma_1} | V_1(\mathbf{k}) | u_m^{\sigma_2} \rangle \langle u_m^{\sigma_2} | V_3(\mathbf{k}) | u_n^{\sigma_1} \rangle + h.c.}{E_n^{\sigma_1} - E_m^{\sigma_2}}, \quad (1.10)$$

where the sum over m, σ_2 includes all states which are not equal to n, σ_1 .

Even though the latter term of Eq. ?? is of higher order in the perturbation theory, it usually has the same order of magnitude as the former. This can be understood from the previous discussion on the origin of various terms in Eq. ??, and in particular what fields contribute to V_2 or V_3 . For this to be true, however, it is important that the orbitals u_n , and u_m in the second term have contributions that originate from an atom with a strong spin-orbit coupling. From the point of view of symmetries, another requirement for the second term to be nonzero is that u_n and u_m have contributions that have different parity, since \mathbf{p} is odd in spatial coordinates, $\mathbf{k} \cdot \mathbf{p}$ is only non-zero when one of the orbitals is odd with respect to a spatial direction and the other even. One example could be a p_y orbital and a $s-p_z$ hybridized one, which would be created by the ferroelectricity with electric polarization along the z -axis (add

drawing? add hopping matrix?).

1.3 Orbital Rashba Effect

Unlike the purely relativistic Rashba-Bychkov effect, the orbital effect combines strong atomic SOC with the generation of nonzero orbital angular momentum (OAM) through electrostatic means. This contribution, therefore, is not limited by the small prefactors of Eq. ???. As will be explicitly shown below, electric dipole matrix element s can cause Bloch functions to acquire nonzero OAM when any electric field is present (e.g. from electric polarization), and vice versa Bloch functions with nonzero OAM acquire nonzero electric dipoles between unit cells[Petersen2000, Park2011, Go2016]. This leads to two separate effects.

Firstly, when atomic SOC is included, OAM is unquenched at the high symmetry k-points. This leads to a correction to the band dispersion that varies linearly with \mathbf{k} . Secondly, even without including the contribution of the atomic SOC, the OAM of the Bloch functions to appear in a chiral texture as one moves away from the high-symmetry k-point, similarly to how the relativistic Rashba effect leads to a chiral spin texture. If one then includes the atomic SOC from Eq. ???, this linear-in-k l will lead to a linear variation of the energy with either positive or negative slope, depending on the spin orientation.

We now proceed by giving a pedagogical derivation of this mechanism based on a tight-binding model [Petersen2000, Go2016].

1.3.1 Tight-Binding model

The tight-binding model is defined on a 2D square layer with one atom per unit cell, and four Wannier orbitals on the atom. We assume that these orbitals are gaussians the form $s(\mathbf{r}, \mathbf{n}) = e^{-\frac{|\mathbf{r}-\mathbf{n}\alpha|^2}{a_0^2}}$, $p_\alpha(\mathbf{r}, \mathbf{n}) = \alpha e^{-\frac{|\mathbf{r}-\mathbf{n}\alpha|^2}{a_0^2}}$ with $\alpha = x, y, z$, and \mathbf{n} denoting the unit cell indices $\mathbf{n} = (n_x, n_y)$. The reason for choosing gaussians is to make solving the overlap integrals more easy, it does not lead to any qualitative changes to the derivation below. To simplify notation below, we omit \mathbf{r} and write $|\alpha^0\rangle = |\alpha\rangle$. The bare tight-binding Hamiltonian is denoted as \hat{H}_0 and includes the usual hopping parameters due to overlap $t_{\alpha\beta}^{ij} = \int d\mathbf{r} w_i^\alpha(\mathbf{r})^* (\frac{P^2}{2m} + V(\mathbf{r})) w_j^\beta(\mathbf{r})$. To mimick the inversion symmetry breaking in ferroelectric materials (i.e. with a polar space group), an electric field perpendicular to the layer (z direction) is applied. This allows extra hopping terms associated with $\hat{H}_{isb} = e(\hat{\mathbf{d}} \cdot \mathbf{E})$, with $\hat{\mathbf{d}}$ the electric dipole moment:

$$\langle s | \hat{H}_{isb} | p_z \rangle = 2eE_z \theta_z^n \quad (1.11)$$

$$\langle p_z | \hat{H}_{isb} | p_x(\mathbf{n}) \rangle = eE_z \theta_z^n n_x \quad (1.12)$$

$$\langle p_z | \hat{H}_{isb} | p_y(\mathbf{n}) \rangle = eE_z \theta_z^n n_y \quad (1.13)$$

with $\theta_z^n = -ae^{-\frac{1}{2}\left(\frac{a|\mathbf{n}|}{a_0}\right)^2} \frac{\pi^{\frac{3}{2}}}{16\sqrt{2}}$, other terms of \hat{H}_{isb} are zero. Fig. ?? shows pictorially how these terms arise from the electric dipoles between the shifted orbitals.

Solving the tight binding model for $k = 0$, one can treat \hat{H}_{isb} as a perturbation on \hat{H}_0 due to the smallness of E_z , leading to a hybridization between the

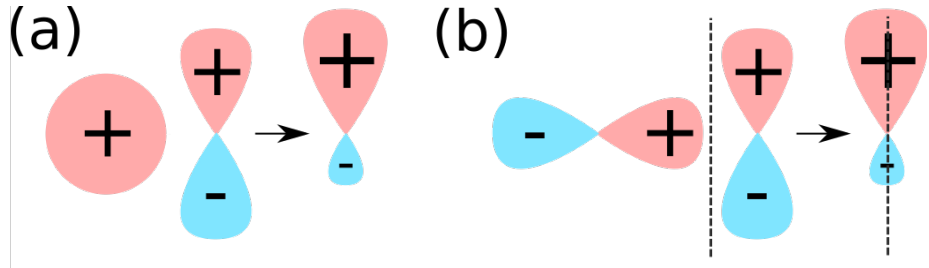


Figure 1.3: **Overlap dipoles.** (a) On-site dipole from s and p_z hybridization, (b) Dipole due to overlap of shifted p orbitals, the dashed line signifies a unit cell boundary.

s and p_z orbitals:

$$|\tilde{p}_z\rangle = |p_z\rangle + \frac{\langle s|2eE_z\theta_z^n|p_z\rangle}{\varepsilon_z - \varepsilon_s} |s\rangle \quad (1.14)$$

$$|\tilde{s}\rangle = |s\rangle + \frac{\langle p_z|2eE_z\theta_z^n|s\rangle}{\varepsilon_s - \varepsilon_z} |p_z\rangle, \quad (1.15)$$

where $\varepsilon_s = \langle s|\hat{H}_0|s\rangle$ and $\varepsilon_z = \langle p_z|\hat{H}_0|p_z\rangle$. In order to proceed, we only treat the important kinetic energy part of \hat{H}_0 and rewrite it in terms of this hybrid \tilde{p}_z orbital in the central unit cell and the shifted p_x, p_y orbitals, leading to:

$$\langle \tilde{p}_z | \hat{H}_0 | p_x(\mathbf{n}) \rangle = \frac{2eE_z\theta_z^n}{\varepsilon_z - \varepsilon_s} \langle s | \frac{-\nabla^2}{2} | p_x(\mathbf{n}) \rangle \quad (1.16)$$

$$= \frac{4eE_z(\theta_z^n)^2}{\varepsilon_z - \varepsilon_s} n_x (-5 + a^2 |\mathbf{n}|^2) \quad (1.17)$$

$$\langle \tilde{p}_z | \hat{H}_0 | p_y(\mathbf{n}) \rangle = \frac{4eE_z(\theta_z^n)^2}{\varepsilon_z - \varepsilon_s} n_y (-5 + a^2 |\mathbf{n}|^2) \quad (1.18)$$

To construct $\hat{H}_0(\mathbf{k})$ and $\hat{H}_{isb}(\mathbf{k})$, one can fourier transform the Wannier Functions:

$$|\alpha(\mathbf{k})\rangle = \frac{1}{\sqrt{N}} \sum_{\mathbf{n}} e^{i\mathbf{k}\cdot\mathbf{n}} |\alpha(\mathbf{n})\rangle \quad (1.19)$$

i with α one of the aforementioned orbitals, \mathbf{k} written in terms of crystalline coordinates ($\frac{2\pi}{a}$), and N denoting the total amount of unit cells in the material. This results in:

$$\hat{H}_0(\mathbf{k}) + \hat{H}_{isb}(\mathbf{k}) = \sum_{\mathbf{n}} e^{i\mathbf{k}\cdot\mathbf{n}} (\hat{H}_0(\mathbf{n}) + \hat{H}_{isb}(\mathbf{n})) \quad (1.20)$$

$$= \sum_{\mathbf{n}} i \sin(\mathbf{k} \cdot \mathbf{n}) (\hat{H}_0(\mathbf{n}) + \hat{H}_{isb}(\mathbf{n})) + k\text{-even terms}, \quad (1.21)$$

keeping only the $\sin(\mathbf{k} \cdot \mathbf{n})$ part of the exponent since the $\cos(\mathbf{k} \cdot \mathbf{n})$ part does not result in linear-in- k terms, in the small \mathbf{k} expansion below we keep only these linear-in- k terms.

If we then assume that at $k = 0$ the Bloch functions are formed from p_x, p_y, \tilde{p}_z and \tilde{s} orbitals: $|\alpha(\mathbf{k} = \mathbf{0})\rangle = \frac{1}{\sqrt{N}} \sum_{\mathbf{n}} |\alpha(\mathbf{n})\rangle$ a perturbation theory for small

deviations \mathbf{k} away from zero can be written down:

$$|\alpha(\mathbf{k})\rangle = |\alpha\rangle + \sum_{\beta \neq \alpha} \frac{\langle \beta | H_0(\mathbf{k}) + \hat{H}_{isb}(\mathbf{k}) | \alpha \rangle}{\varepsilon_\alpha - \varepsilon_\beta} |\beta\rangle \quad (1.22)$$

Gathering the linear-in- k terms, and assuming $\varepsilon_p = \langle p_x | \hat{H}_0 | p_x \rangle = \langle p_y | \hat{H}_0 | p_y \rangle$, we find

$$|\tilde{p}_x(\mathbf{k})\rangle = |p_x(0)\rangle + \Theta \frac{ieE_z k_x}{\varepsilon_p - \varepsilon_{\tilde{z}}} |\tilde{p}_z(0)\rangle \quad (1.23)$$

$$|\tilde{p}_y(\mathbf{k})\rangle = |p_y(0)\rangle + \Theta \frac{ieE_z k_y}{\varepsilon_p - \varepsilon_{\tilde{z}}} |\tilde{p}_z(0)\rangle \quad (1.24)$$

$$|\tilde{p}_z(\mathbf{k})\rangle = |\tilde{p}_z(0)\rangle + \Theta \frac{ieE_z}{\varepsilon_p - \varepsilon_{\tilde{z}}} (k_x |p_x(0)\rangle + k_y |p_y(0)\rangle), \quad (1.25)$$

with $\Theta = \frac{\pi^{5/2}}{256a^3} \left(-16\sqrt{2} + \frac{3a\pi^{3/2}}{\varepsilon_z - \varepsilon_s} \right)$. Then, using the definition of the OAM operators for p -orbitals:

$$\hat{L}_x = \begin{pmatrix} 0 & 0 & 0 \\ 0 & 0 & -i \\ 0 & i & 0 \end{pmatrix}, \hat{L}_y = \begin{pmatrix} 0 & 0 & i \\ 0 & 0 & 0 \\ -i & 0 & 0 \end{pmatrix}, \hat{L}_z = \begin{pmatrix} 0 & -i & 0 \\ i & 0 & 0 \\ 0 & 0 & 0 \end{pmatrix} \quad (1.26)$$

we find that,

$$\langle \tilde{p}_z(\mathbf{k}) | \hat{L}_x | \tilde{p}_z(\mathbf{k}) \rangle = -2\Theta \frac{eE_z k_y}{\varepsilon_p - \varepsilon_{\tilde{z}}} \quad (1.27)$$

$$\langle \tilde{p}_z(\mathbf{k}) | \hat{L}_y | \tilde{p}_z(\mathbf{k}) \rangle = 2\Theta \frac{eE_z k_x}{\varepsilon_p - \varepsilon_{\tilde{z}}} \quad (1.28)$$

These expressions for $\hat{\mathbf{L}}$ can be filled into the expression for the atomic SOC $\hat{H}_{soc} = \lambda \hat{\mathbf{L}} \cdot \hat{\boldsymbol{\sigma}}$ to find the energy for $|\tilde{p}_z\rangle$:

$$\varepsilon(\mathbf{k}) = \frac{2\lambda\Theta eE_z}{\varepsilon_p - \varepsilon_{\tilde{z}}} (\mathbf{k} \times \boldsymbol{\sigma}) \quad (1.29)$$

which has the form of Eq. ??.

From this qualitative derivation, it is clear that the main reason behind the orbital Rashba effect can be traced back to the observation that Bloch functions with nonzero OAM have electric dipoles that couple to the inversion symmetry breaking electric field. We identified two sources that lead to the effect: the first one comes from the direct overlap dipoles between p_x and p_y orbitals, and the p_z orbital[Petersen2000], the second is due to the hybridization of the s and p_z overlap, and the kinetic energy term between the s and neighboring p_x and p_y orbitals[Go2016]. These two terms are reflected in the two terms that contribute to Θ , and lead to a chiral, linear-in- k texture of the OAM. If there then exists strong atomic SOC, this linear-in- k OAM will couple to the spin and result in the final Rashba-like form of Eq. ??.

There is one final term that contributes to the linear variation of OAM with \mathbf{k} , which is only present when there is an unquenching of the OAM at the high

symmetry point ($|k| = 0$) due to the atomic SOC ???. This is due to the energy gain from \hat{H}_{soc} if the material has orbitals that have $\mathbf{j} = \mathbf{l} + \frac{1}{2}\boldsymbol{\sigma}$. Similar to the above derivation a small- k expansion for orbitals with nonzero OAM can be performed, leading in general to:

$$\langle \alpha | \hat{L}_\gamma | \beta \rangle = i\epsilon_{\alpha\beta\gamma} c_\alpha^* c_\beta \quad (1.30)$$

when α, β, γ designate x, y, z . This means that there has to be at least some admixing of multiple p -orbitals to get nonzero OAM. This leads to the following expansion of the Bloch functions around the high-symmetry $|k| = 0$ point:

$$|\psi(\mathbf{k})\rangle = \sum_{\mathbf{n}, \alpha} c_\alpha(\mathbf{k}) e^{i\mathbf{k} \cdot \mathbf{n}} |\alpha(\mathbf{n})\rangle \quad (1.31)$$

$$= \sum_{\mathbf{n}, \alpha} \left(c_\alpha(0) + \mathbf{k} \frac{\partial c_\alpha(\mathbf{k})}{\partial k} \Big|_{\mathbf{k}=0} \right) (1 + i\mathbf{k} \cdot \mathbf{n}) |\alpha(\mathbf{n})\rangle. \quad (1.32)$$

Focusing on the terms that vary linearly with k , the second term in the c expansion together with the first term in the exponent expansion is exactly the contribution that was discussed before. The final term for the Orbital Rashba effect originates from combining the first term in the c expansion with the second in the exponent expansion, leading to the contribution

$$\varepsilon(\mathbf{k}) = \langle \psi(\mathbf{k}) | \hat{H}_{isb} | \psi(\mathbf{k}) \rangle = i \sum_{\mathbf{n}, \alpha, \beta} c_\alpha^*(0) c_\beta(0) \mathbf{k} \cdot \mathbf{n} \langle \alpha(0) | \hat{H}_{isb} | \beta(\mathbf{n}) \rangle \quad (1.33)$$

$$= ieE_z \frac{-\pi^{5/2}}{8\sqrt{2}a^3} (c_x^*(0)c_z(0)k_x + c_y^*(0)c_z(0)k_y) \quad (1.34)$$

$$= eE_z \frac{\pi^{5/2}}{8\sqrt{2}a^3} (L_y(0)k_x - L_x(0)k_y). \quad (1.35)$$

These expressions show us that, due to $\hat{H}_{soc} = \lambda \hat{\mathbf{L}} \cdot \hat{\boldsymbol{\sigma}}$ and $\hat{H}_{isb} = eE_z d_z$, an additional Rashba-like term appears in the energy dispersion.

With the understanding that one can find Rashba like dispersions, coming not from the usually considered purely relativistic, but also from electrostatic mechanisms. We now look at a concrete example that behaves very similar to the above toy model, GeTe.

1.4 Overview: Germanium Telluride

The space group of GeTe is R3m (#160 in International Tables), with ferroelectric polarization along the threefold rotation z -axis caused by an off-centering of the central Te atom [Rabe1987] as displayed in Fig. ??-(a). The valence and conduction bands are formed mostly by s and p orbitals from Te and Ge, respectively. This, together with the large spin-splitting in the vicinity of the Z point [DiSante2013] as observed from the bandstructure in Fig. ??-(b), lends it as a perfect test-case for the above described mechanisms. Moreover, since it is a bulk material, the relativistic Rashba effects contribute negligibly due to the small potential gradients caused by bulk ferroelectricity. The band structure, presents a distinct large linear spin splitting around the Z point, along the $Z - A$ and $Z - U$ paths. The $Z - \Gamma$ path shows no splitting because the electric

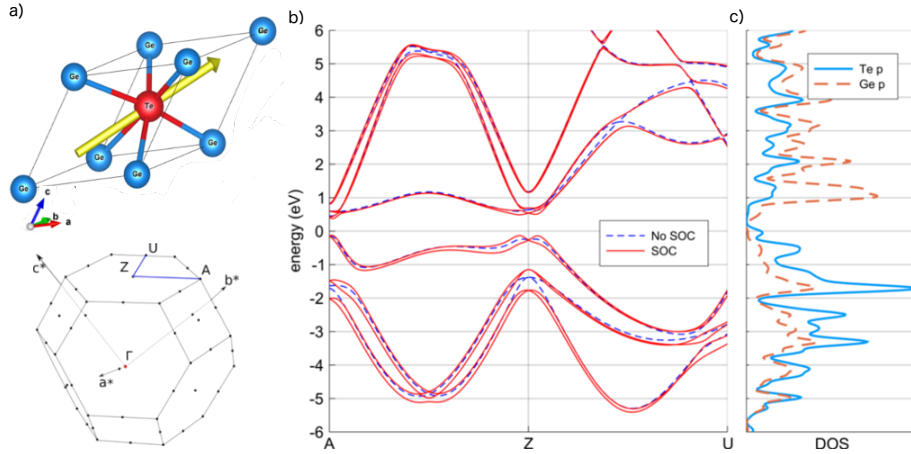


Figure 1.4: (a) Rhombohedral unit cell and Brillouin zone of GeTe, with the polarization direction in yellow. (b) Band structure obtained from a DFT calculation with and without SOC, along the blue path in panel (a). (c) partial DOS for Te and Ge p orbitals computed without SOC.

field is along the z direction, and as shown by the above derivation, only k_x and k_y will show a linear splitting. The density of states (DOS), displayed in Fig. ??-(c), confirms the orbital character of the bands.

1.5 Methods

We performed ab-initio DFT calculations using the Quantum-Espresso software package[**Giannozzi2009**]. In order to confirm the linear varying OAM even when spin-orbit is not included we performed non-relativistic, as well as relativistic calculations. Both were performed using ONCVPSP pseudopotentials, with 30 Ry for the energy cutoff, and 160 Ry for the density cutoff. The reciprocal space was sampled using a 10x10x10 and 6x6x6 Monkhorst-Pack grid for the self-consistent and non-self-consistent calculations, respectively, using an energy convergence threshold of 10^{-7} Ry. Afterwards we used the Wannier90 package [**Mostofi2014AnFunctions**] to perform the Wannierization, using atomic s and p -orbitals on both Ge and Te. This provides us with the tools to analyze the real space properties of Bloch functions such as the dipole moment and OAM.

1.6 Band structure

The bands we will focus on most are the three topmost valence bands. As seen in Fig. ??-(b), these bands have the largest spin-splitting. This suggests that indeed the atomic SOC plays an important rule, seen as these bands are comprised mostly of Te orbitals, and SOC is largest on Te. If one were to fit the dispersion of the topmost band to Eq. ??, it results in a large prefactor $\alpha_R \approx 30.7 \text{ eV}\text{\AA}$ [**DiSante2013**]. As discussed before, a more realistic prefactor would be $\alpha_R = 10^{-6} \text{ eV}$ in the purely relativistic case inside the vacuum.

The last issue with the purely relativistic explanation, which has been confirmed experimentally[Krempasky2015SurfaceSemiconductor], lies in the orientation of the spin polarization of the split bands. According to Eq. ??, the bands should all be split equally and Bloch functions at the same k -point should have the same spin orientations, since their character does not enter Eq. ???. However, as has been shown and will be confirmed by our results below, the orientation depends on the character of the band, more specifically on the value of the total angular momentum j .

1.7 Results and Discussion

The dispersion, OAM, and SAM of the first valence band are shown in the left panel of Fig. ???. Confirming our earlier conclusions, we can see that non-zero, linearly varying OAM is formed as we move away from the high-symmetry Z -point. Moreover, the OAM is perpendicular to both the z -axis and the k vector, as it should be from Eq. ???, and can also be seen from the panels in Fig. ???. This leads e.g. to $l_y = 0$ along the $A \rightarrow Z$ path, where only k_y is nonzero. When atomic SOC is included in the orange and blue graphs, we see the spin-splitting that results from having the spin oriented either along or opposite to the already linearly varying OAM. The unquenching of the OAM at the Z -point when SOC is included is also clearly visible, together with the resulting change in the slope that originates from the corresponding contribution to the dipole moment Eq. ???. This correlation can also be observed in the panel showing the center of mass $\bar{z} = \int_{\text{supercell}} z |\psi(k)|^2$ of the Bloch-functions, which is proportional to the dipole moment around the same reference point.

When we compare this first valence band with the third valence band, shown in the right panel of Fig. ???, we can clearly see the previously discussed issues with the purely relativistic explanation. As stated before, we can note that not only the magnitude but also the sign of the prefactor in Eq. ?? is opposite for these two bands, showcased by the size of the splitting, and by the ordering of the spin-up vs the spin-down splitted part. This is because the character of

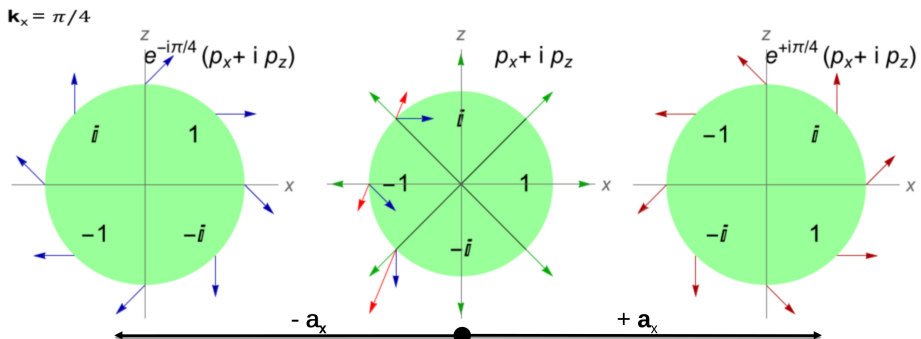


Figure 1.5: Interference between orbitals with nonzero OAM. Three neighboring unit cells are displayed, each with the same $p_x + ip_z$ orbital (thus having nonzero l_y). The wave functions of the left and right unit cells have their phase rotated by the plane-wave part $e^{ik_x R_x}$. The amplitude and phase of the wave function are encoded with the length and polar angle of the arrows.

the first and third valence bands are different. The first valence band is mostly coming from Te $j_{\frac{3}{2}}$ orbitals, whereas the third valence band is predominantly $j_{\frac{1}{2}}$. This causes the orientation of the OAM and SAM to be along each other in the first band, and opposite for the third, as shown in Fig. ???. This then leads to the different ordering of the spin-split bands.

There is one last very interesting feature one can notice from Fig. ?? (c) and (f), that is, the switching of the character (and SAM, OAM orientation) of the bands, very close to the Z point. This is because the crystal field breaks rotational symmetry causing the atomic j to not be a conserved quantity, i.e. there is a mixing between different atomic j orbitals, which varies strongly in this very narrow region around Z .

All these considerations lead to a very nontrivial SAM and OAM texture of the bands as we progress through the BZ.

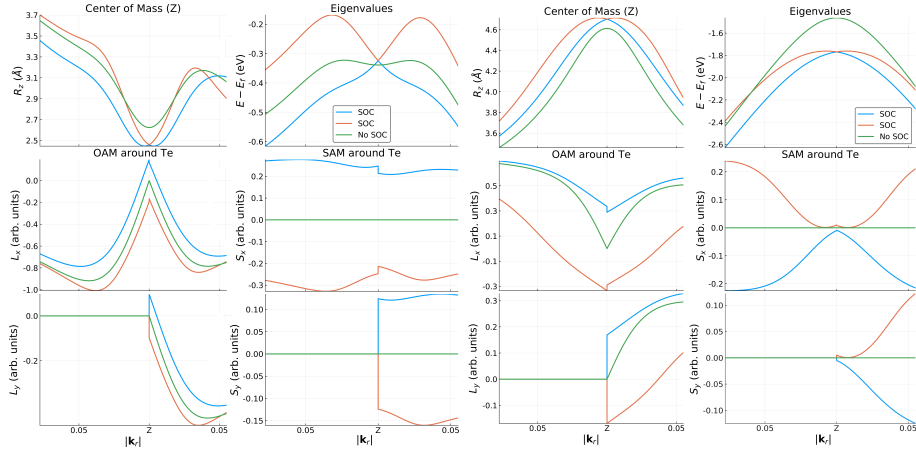


Figure 1.6: Comparison between the real-space observables and energy dispersion in (a) the first and (b) third valence band. The values are plotted in function of the relative distance from the Z point $\mathbf{k}_r = \mathbf{k} - \mathbf{k}_Z$, towards the A and U points. The green graphs denote the values before turning on atomic SOC, whereas the orange and blue graphs denote the two spin-split bands.

1.8 Conclusions

We have explored the microscopic origin of the giant Rashba-like spin splitting in the band structure of bulk ferroelectric GeTe with high atomic SOC. We derived the form of the band dispersion in the Wannier representation, that relates the large spin splitting to the intricate interplay between OAM, atomic SOC, the crystal field and the electric polarization. It turns out that the crucial component, which is not present in the relativistic Rashba effect, is the emergence of a nonzero electric dipole of the Bloch functions due to their OAM. The quantitative analysis based on Wannier functions and atomic-centered approximation confirms this mechanism in GeTe. We find a very good agreement between the proposed band dispersion, Eq. (??), and the dispersions of the first and third valence bands, where the effect manifests itself most clearly.

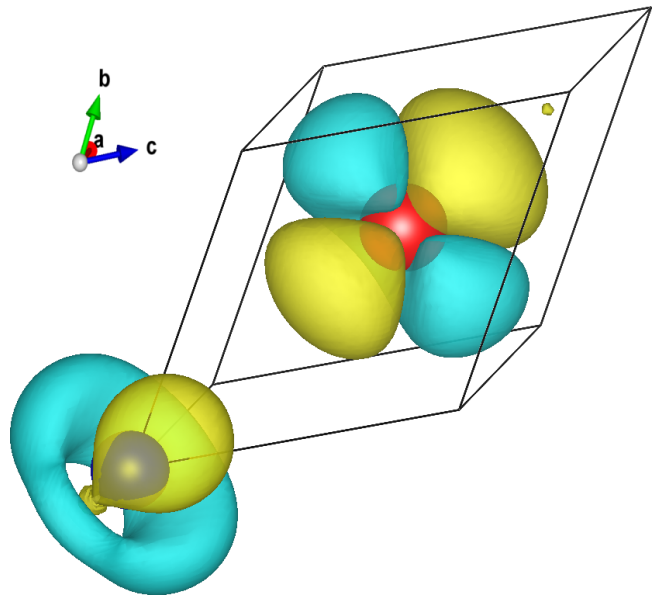


Figure 1.7: The variation of the charge density of the Bloch function of the first valence band $\frac{\partial|\psi(k)|^2}{\partial k}\Big|_{k=Z}$ away from Z towards A . Te and Ge ions are in red and blue, respectively. The charge asymmetry around Ge showcases the nonzero dipole moment along z , which couples to the local electric field near Ge ion.

Ultimately, the results suggest that (1) large ferroelectric polarization, (2) high atomic SOC, and (3) highly symmetric environment producing little OAM quenching could be the design rules for new materials with strong Rashba-like spin splitting. These materials could enable spintronic devices with the much needed electric control of spin polarization.

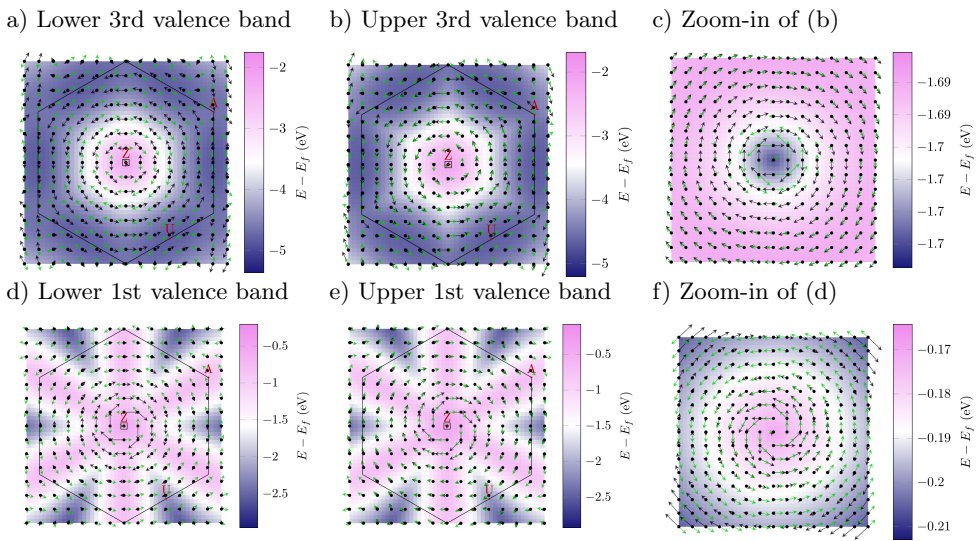


Figure 1.8: OAM and SAM textures around the Z point in the first and third valence bands of GeTe. The black and green arrows show the OAM and SAM textures, respectively. The length of the arrows was chosen separately for clarity in each figure and should thus not be compared. The color maps signify the energy of the bands, relative to the Fermi level. The small box around the Z point indicates the area, magnified in panels (c) and (f). In the zoomed figures (c) and (f) one can observe the change or relative orientation between the SAM and OAM when moving away from the Z point, signifying a change of character between $j = 1/2$ and $j = 3/2$.

Bibliography

- [1] Sebastian Deffner, Christopher Jarzynski, and Adolfo del Campo. “Classical and quantum shortcuts to adiabaticity for scale-invariant driving”. In: *Physical Review X* 4.2 (2014), pp. 1–19. ISSN: 21603308. DOI: 10.1103/PhysRevX.4.021013.
- [2] Eric Fawcett. “Spin-density-wave antiferromagnetism in chromium”. In: *Reviews of Modern Physics* 60.1 (Jan. 1988), pp. 209–283. ISSN: 0034-6861. DOI: 10.1103/RevModPhys.60.209. URL: <http://link.springer.com/10.1134/S0036023613100069%20https://link.aps.org/doi/10.1103/RevModPhys.60.209>.
- [3] Daniel I. Khomskii. *Basic Aspects of The Quantum Theory of Solids*. Cambridge: Cambridge University Press, 2010. ISBN: 9780511780271. DOI: 10.1017/CBO9780511780271. URL: <http://ebooks.cambridge.org/ref/id/CBO9780511780271>.
- [4] N I Kulikov and V V Tugushev. “Spin-density waves and itinerant antiferromagnetism in metals”. In: 954 (1984).
- [5] Patrick Kofod Mogensen and Asbjørn Nilsen Riseth. “Optim: A mathematical optimization package for Julia”. In: *Journal of Open Source Software* 3.24 (2018), p. 615. DOI: 10.21105/joss.00615.
- [6] Bartomeu Monserrat and David Vanderbilt. “Phonon-assisted spin splitting in centrosymmetric crystals”. In: 4 (2017), pp. 1–5. arXiv: 1711.06274. URL: <http://arxiv.org/abs/1711.06274>.
- [7] J. A. Nelder and R. Mead. “A Simplex Method for Function Minimization”. In: *The Computer Journal* 7.4 (1965), pp. 308–313. ISSN: 0010-4620. DOI: 10.1093/comjnl/7.4.308.
- [8] C. W. Nicholson et al. “Ultrafast Spin Density Wave Transition in Chromium Governed by Thermalized Electron Gas”. In: *Phys. Rev. Lett.* 117.13 (2016), pp. 1–5. ISSN: 10797114. DOI: 10.1103/PhysRevLett.117.136801.
- [9] Christopher Rackauckas and Qing Nie. “DifferentialEquations.jl—a performant and feature-rich ecosystem for solving differential equations in julia”. In: *Journal of Open Research Software* 5.1 (2017).
- [10] A Singer et al. “Photoinduced Enhancement of the Charge Density Wave Amplitude”. In: *Physical Review Letters* 117.5 (Nov. 2015). ISSN: 10797114. DOI: 10.1103/PhysRevLett.117.056401. arXiv: 1511.08261. URL: <http://arxiv.org/abs/1511.08261%20http://dx.doi.org/10.1103/PhysRevLett.117.056401>.

- [11] Erik Torrontegui et al. “Shortcuts to Adiabaticity”. In: *Advances in Atomic, Molecular and Optical Physics* 62.September (2013), pp. 117–169. ISSN: 1049250X. DOI: 10 . 1016 / B978 - 0 - 12 - 408090 - 4 . 00002 - 5. arXiv: 1212.6343.
- [12] H. J. Zeiger et al. “Theory for displacive excitation of coherent phonons”. In: *Physical Review B* 45.2 (1992), pp. 768–778. ISSN: 01631829. DOI: 10 . 1103 / PhysRevB.45.768.
- [13] Brian B. Zhou et al. “Accelerated quantum control using superadiabatic dynamics in a solid-state lambda system”. In: *Nature Physics* 13.4 (2017), pp. 330–334. ISSN: 17452481. DOI: 10 . 1038 / nphys3967. arXiv: 1607 . 06503.